Chapter in **Advancing Astrophysics with the SKA – II**

Fast Simultaneous Surveys with On-the-Fly Mapping

Suman Chatterjee*,[1] Sarvesh Mangla**,[2] Sourabh Paul***,[3] Keith Grainge,[3] Matthias Hoeft,[4] Tamera Kassie,[1,5] Joseph J. Mohr,[2] Yvette Perrott,[6] Kristof Rozgonyi,[2] Mario G. Santos,[1,5] Oleg M. Smirnov,[5,7,8] Cyril Tasse[9,10] and Laura Wolz[3]

[1] *Department of Physics and Astronomy, University of the Western Cape, Robert Sobukwe Road, Bellville, Cape Town 7535, South Africa*

[2] *University Observatory, Faculty of Physics, Ludwig-Maximilians-Universität, Scheinerstr. 1, 81679, Munich, Germany*

[3] *Jodrell Bank Centre for Astrophysics, Department of Physics & Astronomy, The University of Manchester, Manchester M13 9PL, UK*

[4] *Thüringer Landessternwarte, Sternwarte 5, 07778 Tautenburg, Germany*

[5] *South African Radio Astronomy Observatory (SARAO), Liesbeek House, River Park, Gloucester Road, Mowbray, Cape Town, 7700, South Africa*

[6] *School of Chemical and Physical Sciences, Victoria University of Wellington, Wellington 6012, New Zealand*

[7] *Centre for Radio Astronomy Techniques and Technologies (RATT), Department of Physics and Electronics, Rhodes University, Makhanda, 6140, South Africa*

[8] *Institute for Radioastronomy, National Institute of Astrophysics (INAF IRA), Via Gobetti 101, 40129 Bologna, Italy*

[9] *GEPI & ORN, Observatoire de Paris, Université PSL, CNRS, 5 Place Jules Janssen, 92190 Meudon, France*

[10] *Department of Physics & Electronics, Rhodes University, PO Box 94, Grahamstown, 6140, South Africa*

E-mail: *`sumanchttrj05@gmail.com`, `6306414@myuwc.ac.za`,
** `mangla.sarvesh@physik.lmu.de`, ***`sourabh.paul@manchester.ac.uk`

© The Authors

The SKAO is a next-generation radio telescope that will transform our understanding of the formation and evolution of radio galaxies, quasars, transients, and other cosmic sources. Surveys conducted on precursor telescopes can inform us about the capabilities and challenges to be overcome in preparation for SKAO science. The MeerKAT Large Area Synoptic Survey (MeerKLASS), is a pathfinder large area survey to probe cosmology using the single-dish H I intensity mapping (IM). MeerKLASS provides an additional wide, high angular-resolution commensal survey by utilizing the "On-the-Fly" (OTF) imaging technique. The survey target is to cover 10,000 sq. degrees in the Southern sky avoiding the Galactic plane, using the UHF-band (544-1088 MHz). The survey aims to achieve an r.m.s. of 25 μJy/beam and 14$''$ resolution. In this chapter we discuss the survey strategy, observational status, the development of the MeerKLASS OTF imaging pipeline and the science prospects of the data products. OTF imaging, which relies upon constant elevation fast scanning, comes with its own set of challenges, such as smearing. Here we detail how we have mitigated them and the current scientific impact. Significantly fast survey speed ($\sim$ 3.5 sq. deg per min), commensality with H I IM survey, deep and large area continuum images make MeerKLASS OTF an economic survey technique. Lessons from this technique will be valuable for the upcoming SKA-Mid, where we expect a better resolution ($< 2''$) and sensitivity ($\sim 7\mu$Jy/beam) of the OTF images with the AA4 configuration. Furthermore, improvements in the correlator will result in negligible smearing effects in the imaging.

1 Introduction

Over the past decade, we have seen multiple large area radio surveys from very low frequencies (*e.g.* 70 MHz, de Gasperin, F. et al. 2023) to as high as 20 GHz (Murphy et al., 2010). It is also becoming evident that the impact of these wide-area radio surveys are undeniable in the field of cosmology, galaxy cluster and large-scale structures in the universe (Alonso et al., 2021; Hale et al., 2023). These large-area surveys are playing a crucial role in understanding the evolution of galaxies, properties of nearby galaxies and magnetic sky. As we start observing with the SKA-Mid and Low, then such wide area surveys are expected to be much deeper.

Before SKA, several of its pathfinder instruments have invested in precursor synoptic surveys to characterise stellar and galaxy population to unprecedented detail (Hurley-Walker et al., 2016; McConnell et al., 2020; Hopkins et al., 2025; Hale and Tabatabaei, 2026). A description of the surveys is provided in Table 1. However, these surveys usually take many years of observations to complete, primarily due to the point-and-track observations strategy. These traditional observational strategies have a significant overhead and a smaller footprint which leads to slow survey speed. Furthermore, different science cases require different amount of resources, for example, neutral hydrogen (H I) intensity mapping (IM) experiments require long observations to beat down noise and other systematics (Harrison et al., 2026), whereas transients surveys require covering a vary large area of sky repeatedly, requiring fast scanning.

To achieve an elevated efficiency of a wide-area multi-epoch survey, it is necessary to rapidly slew the telescope across the sky. The observed data is then collected continuously at a regular interval during this rapid slew of the telescope in what is called " On-The-Fly" (OTF; Mangum et al. 2007; Sawada et al. 2008; Mooley et al. 2018; Chatterjee et al. 2025). The OTF also uses the fact that the next generation telescopes, such as SKA, will have large instantaneous sensitivity. The main scientific aims of a generic wide-area radio survey are to explore the evolution of galaxies, clusters and the large scale structures, search for slow transients and measure magnetic fields through rotation measure synthesis of polarisation data.

In this chapter, we describe the OTF capabilities of SKA-Mid pathfinder MeerKAT [1] that takes advantage of highly sensitive, low-noise receivers and also show the importance of commensal observation planning. MeerKAT consists of 64 × 13.5-m dishes with offset Gregorian optics, providing an unblocked aperture. It is equipped with three receiver bands: UHF (544-1088 MHz), L band (856-1712 MHz), and S band (1750–3500 MHz). Three-quarters of the collecting area is within a dense, 1 km diameter core region, and the remaining dishes are situated around the core, providing a maximum baseline of 8 km. The large number of baselines, wide field of view (2 deg at UHF-band), and low ($\sim$ 20 K) system temperature all combine to make MeerKAT an exceptionally fast and capable synthesis imaging telescope. The correlator can also deliver up to $32,768$ frequency channels, resulting in excellent spectroscopic imaging capabilities and capability for excellent RFI excision.

The MeerKAT Large Area Synoptic Survey (MeerKLASS; Santos et al. 2017) plans to observe $\sim 10,000$ sq. degrees in the Southern sky outside the galactic plane over the next few years.

---

[1] https://www.sarao.ac.za/science/meerkat/

The survey is performed both in the auto-correlation (single dish mode) and the cross-correlation (interferometric mode). With the single dish observations, the survey aims to perform the H I IM up to redshift of $z = 1.44$. MeerKLASS auto-correlations survey aims for a statistical detection of the H I IM signal both in auto-power spectrum and cross-correlation with other surveys (Cunnington et al., 2022; Collaboration et al., 2025; Cunnington et al., 2025, 2026). In this chapter, we discuss a commensal OTF continuum survey with the interferometric visibilities recorded during MeerKLASS observations. The MeerKLASS target sky area has significant overlap with several optical/NIR, wide, galaxy surveys and is expected to provide an invaluable legacy data set.

197 dishes of future SKA-Mid are arranged in a tightly packed central core with three spiral arms extending outward, providing baselines of up to 150 km (Braun et al., 2019). These long separations are crucial for achieving high angular resolution interferometric observations. At its completion, the array will have a total collecting area of 33,000 sq. meters and cover frequencies from 350 MHz to 15.4 GHz, with an aspirational upper limit of 24 GHz. In this chapter, we focus on Band 1 of SKA-Mid that will operate between a frequency range 0.35-1.05 GHz. Our aim here is to explore the possibility of OTF mapping similar to MeerKLASS OTF survey using Band 1 of SKA-Mid.

The chapter is organized as follows. In section 2 we discuss the basic survey strategy implemented for MerrKLASS OTF survey, challenges and the impact of that in data products. section 3 describes the pipeline built for OTF mapping. In section 5 and section 4 we discuss what have been achieved using L and UHF-band of the MerrKAT, respectively. We present our OTF-mapping forecast for SKA-Mid in section 6, and conclude the chapter with a summary of key points in section 7.

2 MeerKLASS OTF formalism

The MeerKLASS scanning strategy is optimised for the single-dish mode (Wang et al., 2021), however, visibilities are recorded for all scans and using the OTF mapping technique, continuum images can be produced from all data. For the rest of this chapter, we will refer to the MeerKLASS OTF data products as “M-OTF”. Each M-OTF observation is made with the full instantaneous bandwidth of the telescope divided into 4096 contiguous frequency channels and with a sampling of $\delta t = 2$s. All four polarization of the visibilities (XX, XY, YX, YY) are recorded to allow images to be made in stokes parameters I, Q, U and V.

2.1 Survey Strategy

A constant elevation fast scanning strategy is adopted to optimise the coverage of the relevant large angular scales and the stability time-scale of the instrument. MeerKAT dishes are moved back and forth to scan in the azimuth (az) direction at a constant elevation (el) with a slew of $\sim$ 10 deg in the sky (Fig. 2). This also minimizes fluctuations in the ground spill and air-mass (Wang et al., 2021). One end-to-end slew is named ‘scan’ in the subsequent text. The telescope speed for a scan is set to $\Theta = 7/\cos(el)\,\mathrm{arcmin\,s^{-1}}$ so that the projected scan speed on the sky is fixed a $7\,\mathrm{arcmin\,s^{-1}}$ which ensures that the telescope pointing does not shift significantly compared to the full-width-half-maximum (FWHM) of the primary beam (at UHF − band $\sim$ 2 deg) during a single time dump (2-second, a snapshot). One ‘box’, an area of approximately 300 sq. deg., is observed for about 2 hours (an‘epoch’). The same box is observed with a rising sky and setting sky as these

Table 1: A non-exhaustive summary of recent large area low-frequency surveys (see also Figure 1). We have attempted to provide a fair comparison of sensitivities and resolutions, but we note that both the sensitivity and resolution achieved vary within a given survey.

Survey	Resolution ($''$)	Noise (μJy/beam)	Frequency (MHz)	Declination	Area (degree^2)
TGSS ADR (Intema et al. 2017)	25	3500	140–156	$\delta > -53°$	36,900
GLEAM (Wayth et al. 2015)	150	5000	72–231	$\delta < +25°$	24,831
LOTSS DR2 (Shimwell, T. W. et al. 2022)	6	83	120–168	$\delta > +15°$	5,635
RACS-Low (Hale et al. 2021)	18	260	743.5–1031.5	$\delta < +30°$	30,480
RACS-Mid (Duchesne et al. 2023)	11.2	140	1151.5–1439.5	$\delta < +49°$	36,200
RACS-High (Duchesne et al. 2025)	11.8	195	1511.5–1799.5	$\delta < +48°$	37,000
EMU (Norris et al. 2011, Hopkins et al. 2025)	15	20-30	800–1088	$\delta < +30°$	20,626
MALS (Gupta et al. 2016, Wagenveld, J. D. et al. 2024)	7.7	10	856–1712	$\delta < +30°$	4,344
SUMSS (Mauch et al. 2003)	45	1500	843	$\delta < -30°$	8,000
NVSS (Condon et al. 1998)	45	450	1400	$\delta > -40°$	33,000
VLASS (Lacy et al. 2020)	2.5	70	2000 – 4000	$\delta > -40°$	33,885
MeerKLASS (UHF) (Paul et al. 2025)	14[23.3]^a	25	580–1015	$\delta < +10°$	10,000
MeerKLASS (L) (Mangla et al. 2025)	11[14]^b	20	856–1712	$\delta < +10°$	500

a: The target resolution is $14''$, whereas '[]' shows the average beam after the smearing correction, where beam = $\sqrt{b_{\rm maj} b_{\rm min}} = \sqrt{32'' \times 17''}$.

b: Same as mentioned in 'a', where beam = $\sqrt{25'' \times 8''}$.

scans cross each other and provide us with good sky coverage in the region of overlap (Fig. 2). This strategy is adopted to accommodate the challenging requirements for the total power H I IM observations (Wang et al., 2021).

Figure 2 shows an example scenario where one rising and one setting epochs are observed for one 'box'. We perform about 26 repeated observations for each box to meet the requirements of H I IM

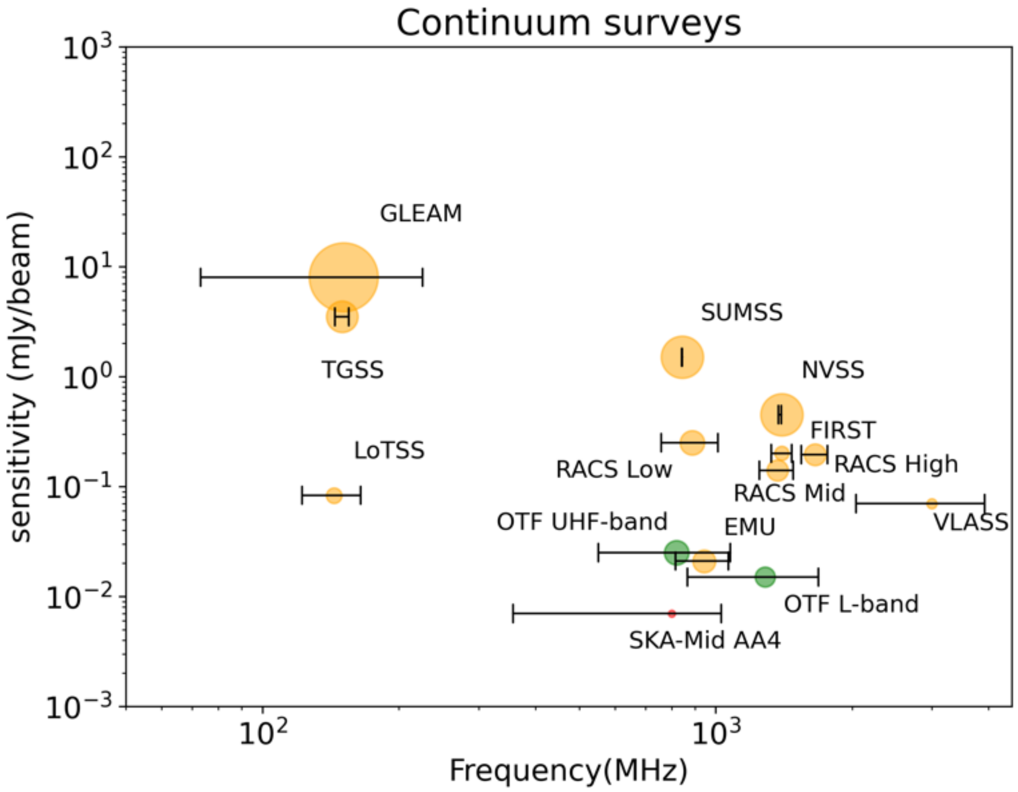

Figure 1: A summary of recent large area low-frequency surveys in including their sensitivity, frequency, and resolution (see Table 1). The size of the markers is proportional to the square root of the survey resolution. The horizontal lines show the frequency coverage for surveys. The green circles show the expected sensitivity and resolution of MeerKLASS OTF surveys without smearing incorporated. Red circle show the expected resolution and the sensitivity achievable using OTF mapping with SKA-Mid AA4 configuration.

observations. Figure 3 shows a prediction of our pipeline when combining (mosaicking) the 2-second pointings for the combination of one rising and one setting epochs from one observation box. To estimate this we assumed a Gaussian primary beam with FWHM = 2°, which is independent of frequency. In practice primary beam varies with frequencies and contain side lobes; however, for simplicity, we ignore this here. We perform a convolution of the primary beam and the scanning pattern shown in Figure 2 to compute this. The beam weighted exposure time gives us an optimistic estimate of the expected integration time at different RA-DEC while combining all the different 2-second measurements from an observation box. Following the radiometer equation, the expected average r.m.s. achievable in continuum (σ_N) change with the integration time by an inversely proportional relation ($\sigma_N \propto 1/\sqrt{\delta t}$) and as a consequence we expect the M-OTF continuum images to be most sensitive in the hexagonal region in the middle (see Figure 2) where the average time spent is larger when compared with the edges of the observation box. However, as we continue with the survey the edges from different observation boxes are expected to overlap and provide us with relatively uniform r.m.s. throughout the survey area. Figure 4 illustrates the planned sky coverage of the ongoing MeerKLASS survey (green dashed outline). The grey-scale background

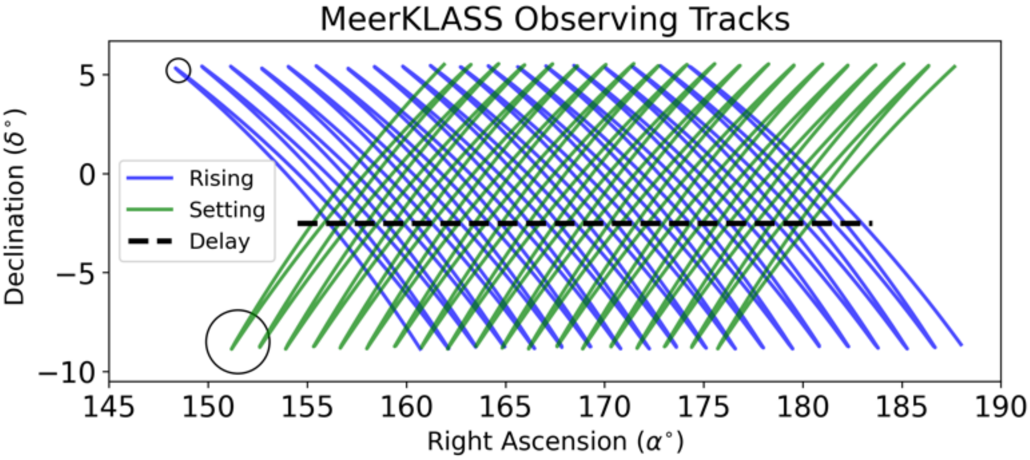

Figure 2: An example of MeerKLASS constant elevation observing strategy where “rising" and “setting" epochs are shown in blue and green, respectively. L and UHF-band primary beam FWHM at the nominal frequencies are shown using circles. Each epoch lasts approximately 100 mins. This region is called a ‘box’ according to our naming conversion. The horizontal dashed line passing through the center of the scanning pattern marks the sky region where the delay for the visibilities are set while the dishes perform fast scanning.

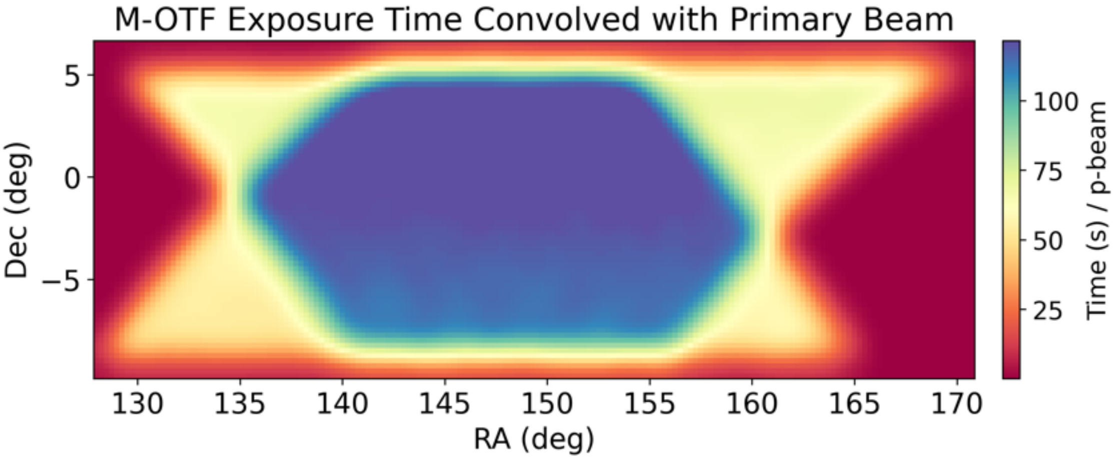

Figure 3: The figure shows the effective exposure time convolved with the primary beam, assuming every 2-second snapshot contributes to the imaging. Here we have considered a combination of one rising and one setting scan.

map shows Galactic synchrotron emission, highlighting the low-foreground regions targeted by the survey. The foreground heat map represents the beam-weighted exposure time, demonstrating how the overlapping scanning strategy achieves uniform sensitivity across a large area of the southern sky.

In the current setup of MeerKAT, we are able to measure interferometric visibilities in two different methods. 1) The delay center of the observation can be set at a fixed RA-DEC for each scan, and during that scan, that fixed RA-DEC is used for sidereal tracking. 2) The delay center can be set to a fixed azimuth-elevation (az-el) at the beginning of the constant elevation scans and remain fixed

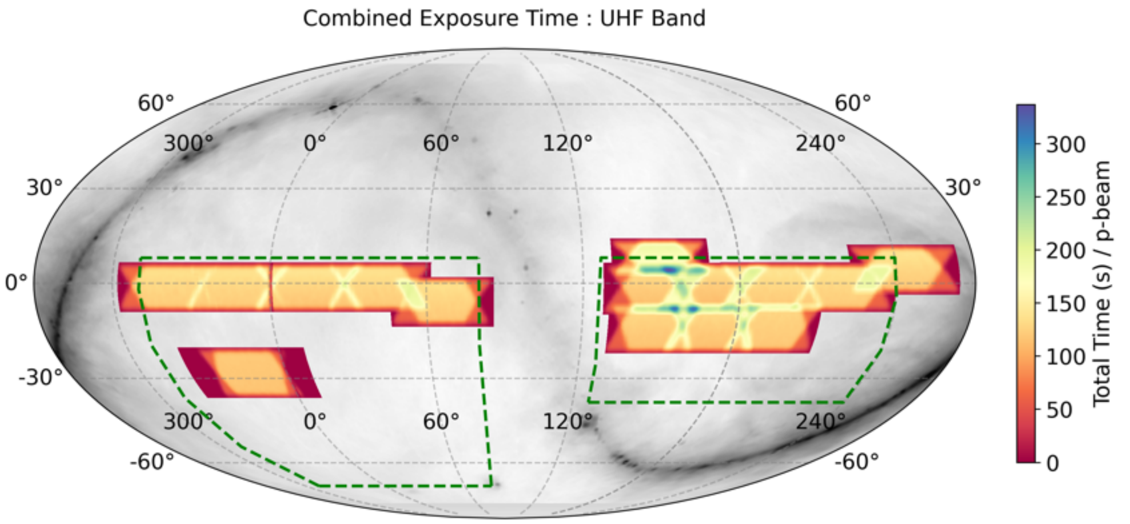

Figure 4: The green dashed lines show the planned survey region for the MeerKLASS. Background shows the Haslam map at 408 MHz (Haslam et al., 1982), we avoid observing the region close to Galactic plane. The effective exposure time convolved with the primary beam is shown for the region observed till the end of 2025. Here we have considered a combination of one rising and one setting scan to compute the effective exposuer time.

throughout the fast scanning observation without sidereal tracking. These two setups introduce unique challenges to process and provide good quality science ready data products. We discuss how we have overcome these challenges in subsequent sections. It is worth mentioning that these setups were an unfortunate necessity due to the capabilities of MeerKAT correlators and future SKA-Mid will allow sidereal delay tracking during fast scanning observations. As a consequence, we expect these issues to be absent during SKA-Mid observations.

2.2 M-OTF with delay fixed in Sky coordinates

This is a newly implemented M-OTF setup that allows to perform tracking of a RA-DEC positions that drift through the middle of the current linear scan (see Figure 2). This results in a separate fixed RA-DEC target for each scan line, which is tracked for the duration of the scan. This survey mode has been developed recently and is still undergoing testing.

2.2.1 Theoretical formulation

In a radio interferometric observation visibilities are the primary measured quantity. Considering an observation at time t and frequency ν the visibility function for two antennas can be written as,

$$\mathcal{V}\left(b,\nu,t\right) = \int d\Omega\, \mathcal{I}\left(\hat{r},\nu,t\right) \mathcal{B}\left(\hat{r},\nu,t\right) e^{-2\pi i \frac{\nu}{c} b(t)\cdot\hat{r}}. \tag{1}$$

Here $\mathcal{I}\left(\hat{r},\nu,t\right)$ is the specific intensity of the sky at an arbitrary direction $\hat{r}$, $\mathcal{B}\left(\hat{r},\nu,t\right)$ is the primary beam response of the antennas along $\hat{r}$ and $b(t)$ is the baseline vector between two antennas. For convenience, we assume a coordinate system that is fixed to the celestial sphere. In this case, we consider fixing the delay in the sky coordinate while the telescope is performing a fast scan. In

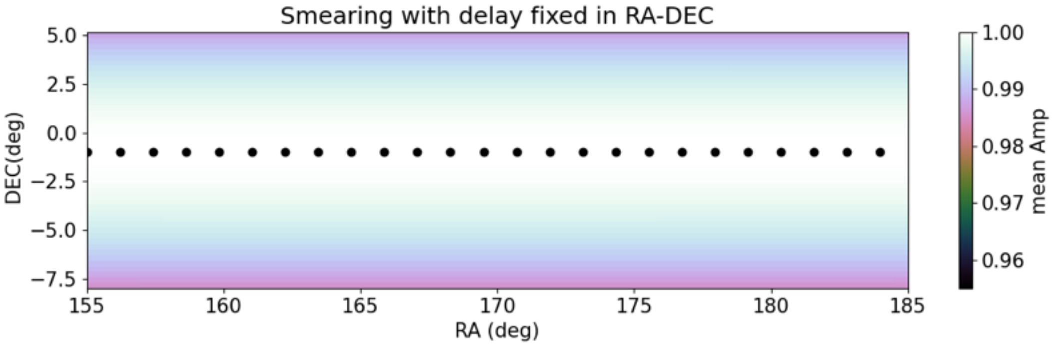

Figure 5: This shows the impact of the M-OTF smearing on a point source average amplitude as a function of RA-DEC when the delay is fixed at a sky coordinate.

case of M-OTF observation, let us assume that the correlator is adding delay tracking as described above towards a sky direction $\hat{r}_d$ (and that this is continuous for simplification). When averaging over time and frequency, we get:

$$\mathcal{V}\left(b,\nu_m,t_m\right)=\int d\Omega\,\mathcal{I}\left(\hat{r},\nu_m,t_m\right)\mathcal{B}\left(\hat{r},\nu_m,t_m\right)\times e^{-2\pi i\frac{\nu_m}{c}b(t_m)\cdot[\hat{r}-\hat{r}_d]}\,\mathrm{sinc}(\delta\Psi)\,\mathrm{sinc}(\delta\Phi), \quad (2)$$

where t_m and ν_m are the central values of the intervals. The averaging in time and frequency introduces smearing where the smearing coefficients, $\delta\Psi$ and $\delta\Phi$ are expressed as (Smirnov, 2011; Tasse et al., 2018),

$$\delta\Psi=\pi\delta t\frac{\nu_m}{c}\frac{db}{dt}|_{t=t_m}\cdot[\hat{r}-\hat{r}_d] \quad (3)$$

$$\delta\Phi=\pi\frac{\delta\nu}{c}b(t_m)\cdot[\hat{r}-\hat{r}_d]. \quad (4)$$

2.2.2 *Simulated predictions*

To investigate the impact of the smearing and assess the accuracy of the theoretical formulation, we simulate M-OTF observations for a single source of 1 Jy at the phase-center without adding system noise. The simulations were performed around a fixed arbitrary time T_0. To capture the smearing effect, we generate visibilities with an artificially high time resolution of $\tilde{\delta t}=\delta t/100$ and frequency channel width of $\tilde{\delta\nu}=\delta\nu/100$ for a bandwidth of 1 MHz. An unitary primary beam is assumed. We then vector sum these visibilities to the equivalent channel and time resolution to that of the actual observation. Figure 5 shows the result, for one such block of observation, where the black points show the delay centers and the average amplitude is plotted in color-bar for a range of RA-DEC values. If there were no smearing present in the observation, we expect the average amplitude value to be unity everywhere whereas we see the minimum value of the amplitude can go upto 0.97 which implies about 3% loss of flux towards the edge of the block. This can be mitigated by correcting the visibilities by the relation introduced in Equation 4.

2.3 M-OTF delay fixed in Azimuth and Elevation

2.3.1 Theoretical formulation

The primary drawback of the current MeerKLASS setup is its inability to track the sky during the integration time (δt) due to fixed azimuth-elevation delays. As the sky rotates, this lack of tracking causes a baseline-dependent loss of phase coherence during averaging. This manifests as irreversible smearing in the M-OTF images that cannot be fixed with post-hoc delay corrections (Chatterjee et al., 2025).

The mathematical details of the smearing effect are described in Chatterjee et al. (2025), and the smearing can be quantified by

$$\delta\Psi = \pi\delta t \frac{\nu_m}{c}\frac{db}{dt}|_{t=t_m} \cdot \hat{r}_p \tag{5}$$

$$\delta\Phi = \pi\frac{\delta\nu}{c} b(t_m) \cdot [\hat{r}_p - \hat{r}_c(t_m)], \tag{6}$$

where $b(t_m)$ is the baseline vector at time t_m, $\hat{r}_p$ the source position and $\hat{r}_c(t_m)$ the time dependent delay position. Here $\delta t = 2$seconds and, $\delta\nu = 133$ and 209kHz for UHF and L-band respectively. Since the delay applied within the time resolution δt remains constant, we expect the sinc functions will reduce the amplitude of the source flux due to phase errors (smearing). The smearing can be estimated by the factor $\mathrm{sinc}(\delta\Psi)\mathrm{sinc}(\delta\Phi)$ defined in Equation 5 and 6. Using this we can construct an effective smeared PSF that can be used to create an accurate sky model from the smeared M-OTF observations (see section 3.4).

2.3.2 Simulated predictions

The key difference between a tracking and current M-OTF observation is that the delays are not corrected for Earth's rotation within the integration time and as a consequence, the aforementioned source moves away from the delay center (which ideally should be the same as the phase center). The point source is at the phase-center of the observation at the time T_0, and incorporating the Earth's rotation, visibilities simulated between $T_0 - \delta t/2$ to $T_0 + \delta t/2$ are summed to obtain the final visibility. Since the delay applied within the time resolution δt remains constant, we expect the summed visibility amplitude at large baselines to decrease from unity due to phase errors. This is in contrast to a tracking observation where we expect phases of all the component visibilities to be the same and so the amplitudes of the visibilities to be unity at all the observed baselines.

During M-OTF observations, the antennas are steered ±5° rapidly at a constant elevation around the central azimuth. This introduces a further variation in the declination and impact of this is shown in the figure 6. Here the simulation is performed for a fixed elevation of 40°. The variation of the declination depends upon the elevation and the time of observation. Both being fixed in the simulation the effect of the smearing is primarily associated with the variation in declination due the steering of the antennas and the change in the projected baselines. These simulations give us an idea about the degree of impact on the images due to the smearing.

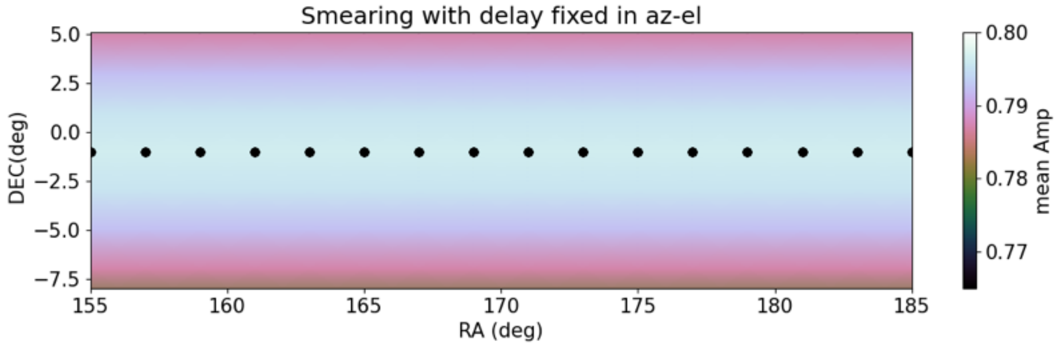

Figure 6: This shows the impact of the M-OTF smearing on a point source average amplitude as a function of steering in azimuth at a fixed elevation of 40°.

3 M-OTF pipeline and imaging

Processing of the M-OTF visibilities is different compared to the traditional tracking observation. In this section, we describe the process of flagging and calibration in our pipeline for the observed visibilities.

3.1 Flagging

3.1.1 Rogue antenna flagging

The MeerKLASS scanning strategy involves driving the antennas back and forth rapidly in azimuth while the elevation remains fixed. However, we have found that during these fast scanning some of the antennas can fall behind or just stop moving for some time. It is important that we identify these misbehaving or 'rogue' antennas and flag them from the visibilities. To identify these rogue antennas we compare the pointing of each antenna as a function of time with the median of the antenna pointing distribution. If an antenna deviates more than $\delta\theta \sim 0.1^\circ$ from the median pointing of the antennas at any time stamp, it is flagged.

3.1.2 RFI flagging

Radio Frequency Interference (RFI) is emitted from various sources, terrestrial or orbital, and creates a nuisance for ground-based radio observations. Since MeerKAT has a large effective collecting area of approximately 1960.88 square meters, it has high sensitivity and as the sensitivity of the instruments increases, so does the sensitivity to unwanted signals (Harper and Dickinson, 2018; Engelbrecht et al., 2024). Primary RFI contributors to the MeerKLASS observations are Digital TV (UHF), GSM (Mobile phones) (UHF + L-band), Aircraft transponders, GPS, GLONASS, Galileo and Inmarsat[2]. MeerKAT has RFI mitigation systems to prevent RFI before and during the observation (Jonas and MeerKAT Team, 2016). However, as even the best RFI mitigation methods cannot completely prevent all RFI (Baan, 2010), we must employ methods to reduce the effect of RFI after observation.

---

[2] https://skaafrica.atlassian.net/wiki/x/AQAzEg

After flagging the rogue antennas, we process the calibrator and the scan data through our RFI flagging step. The RFI flagging is performed using the `TRICOLOR` package (Hugo et al., 2022), which implements the ‘sumthreshold’ algorithm (Offringa et al., 2010) optimised for MeerKAT. Considering the UHF-band, we see that the frequency window between 580 - 880 MHz is relatively clean with the flag fraction mostly below 0.15. We found the pipeline is able to remove all the major RFI contamination successfully; however, the RFI environment somewhat changes in time, and as a result, the flag fraction can change between one epoch to another for the same observation box.

3.2 Calibration

The current MeerKLASS calibration strategy relies upon a primary, a secondary and a polarisation calibrator. It is not efficient to stop and steer the telescope for calibration observation once the constant elevation scanning starts. Due to this limitation, we observe the calibrators at the beginning and toward the end of an epoch for a given observation box. We use `CARACal`[3] (Józsa et al., 2020) to produce calibration tables from the primary, secondary and polarisation calibrators. We follow a ‘standard’ calibration strategy to solve the delays, band-passes and gains, and calibrate for the absolute flux using the primary calibrator source. Most of the MeerKLASS observations are preformed at night and are significantly distant from the solar activity. Hence, we expect the ionospheric effects to be subdominant and these have been ignored throughout this paper.

3.3 Phase Center Correction

The delays applied in the correlator are calculated for a particular RA-DEC or a single az-el, whereas the antennas point in a direction which is different from the delay center. This step in our pipeline splits the whole measurement set (MS) file of an observation epoch into multiple 2s snapshot files, each of which contains visibilities taken at a single, unique timestamp. Further, it applies a phase-rotation to the visibilities from the observed delay center to the pointing center for every visibility integration time (δt). We use the `CHGCENTER` task in `WSClean`[4].

Finally, we use “on-the-fly" calibration option in `CARACal` to apply the calibration tables obtained previously (Section 3.2) on each 2s delay rotated snapshot measurement sets. At the end of this step, the calibrated snapshot visibilities are stored on disc and further processed for imaging.

3.4 Imaging

The immediate and most intuitive product for M-OTF are the 2s total intensity (Stokes I) snapshot images. The 64 dishes of the MeerKAT, in conjunction with a cryogenically cooled receiver system, provide excellent snapshot u-v coverage and low system temperature (T_{sys}), which are essential for imaging the 2s snapshots. To achieve better depth sensitivity and image fidelity, we have chosen to perform visibility plane mosaicking (joint deconvolution) for the M-OTF images (see Chatterjee et al. 2025). We use `DDFacet` (Tasse et al., 2018) to perform smearing correction and imaging the M-OTF visibilities with mosaicking in the visibility plane. The purpose of using an algorithm that relies on faceting is to approximate a wide FoV with many narrow field images.

---

[3] https://caracal.readthedocs.io/

[4] https://wsclean.readthedocs.io/

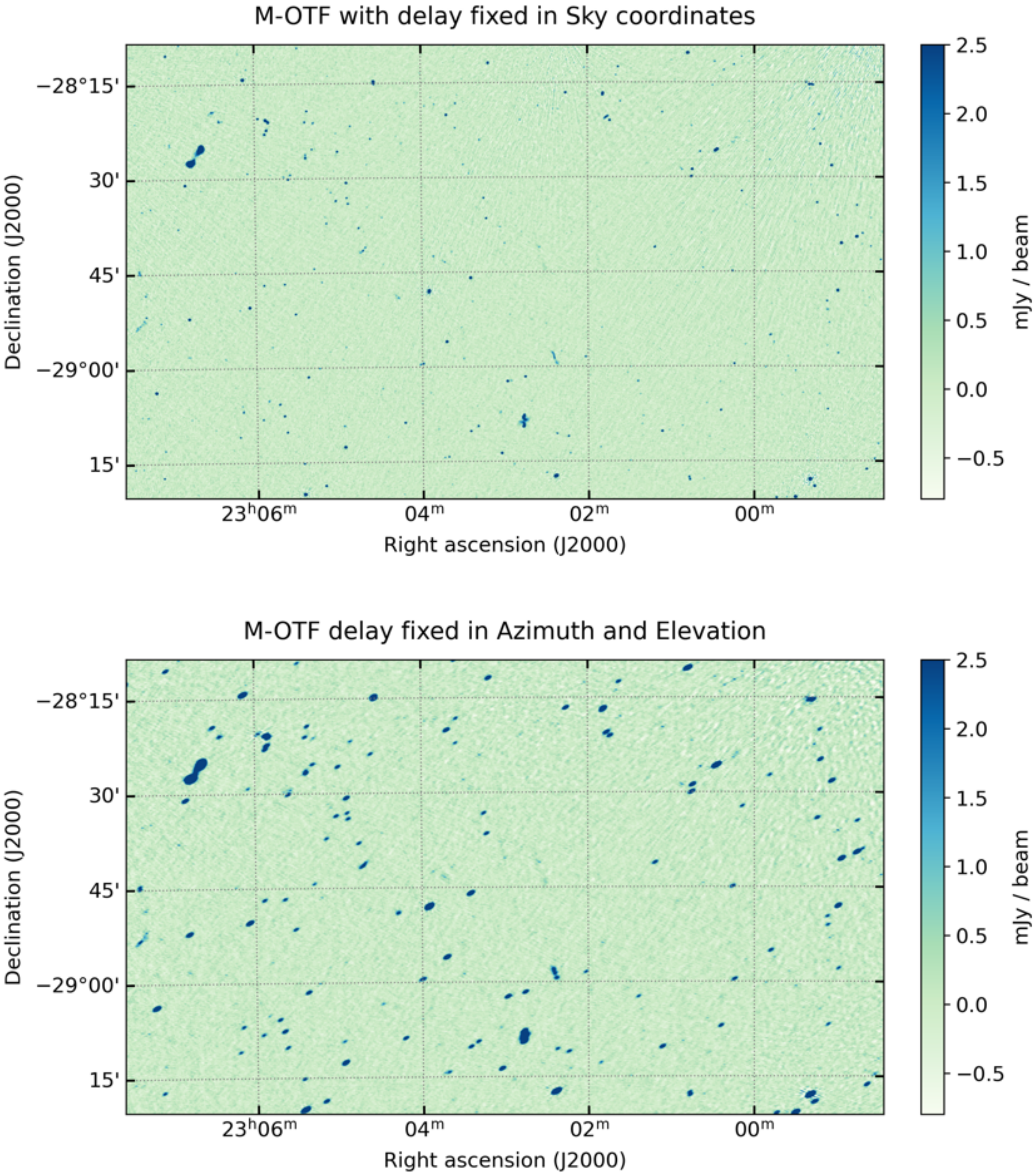

Figure 7: These show the M-OTF final image products in the UHF band. Top panel show the image quality for the newly implemented setup where the delay for each scan is set in the sky coordinate and the correlator performs sidereal tracking to accommodate Earth's rotation. The bottom panel shows the image quality for the setup where the delay is fixed at an az-el and the telescope doesn't tracks the Earth's rotation.

In this chapter, we show the image products using both the MeerKAT set ups. The top panel of the Figure 7 shows the image from the newly implemented setup for M-OTF with delay fixed at sky coordinate with sidereal tracking, whereas the bottom panel shows the resulting image from M-OTF delay fixed at an az-el without sidereal tracking. Considering the top panel, we have used observations from one epoch only, where we have combined 31 snapshots per square degrees to

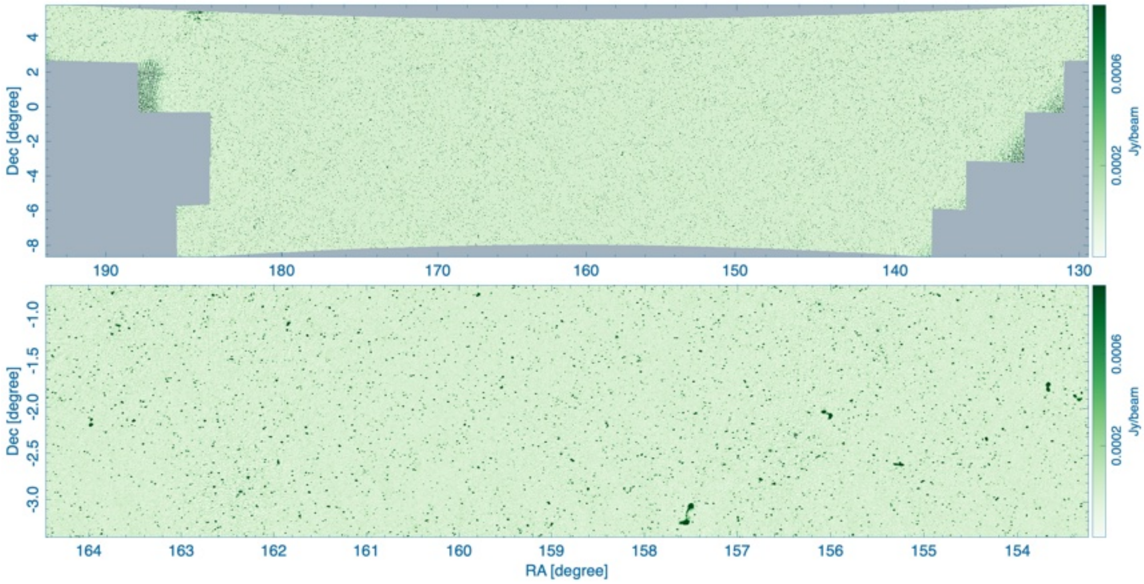

Figure 8: Overview of the mosaic and image quality across the MeerKLASS UHF survey area used in DR1. The top panel shows the full ~800 deg^2 continuum mosaic constructed from 89 tiles at the UHF band centre (816 MHz). Bottom panel displays a zoomed in view of the survey's center region.

construct a $3.2^\circ \times 3.2^\circ$ image and here we show a central cutout of $1^\circ \times 1^\circ$. Using the visibility plane mosaic,we are able to achieve a continuum resolution of $14''$ and a noise of $\sim 163\mu\mathrm{Jy/beam}$ in the UHF-band.

The bottom panel of Figure 7 shows a visibility plane mosaic image from the M-OTF observation where the delay is fixed in *az-el* and the correlator does not track Earth's rotation. We used the DDFacet to correct for the smearing during the deconvolution with a smeared PSF. We are able to achieve a continuum resolution of $32'' \times 15''$ and a noise of $\sim 160\mu\mathrm{Jy/beam}$ in the UHF-band. The resolution is significantly poorer when compared with newly implemented observing mode due to smearing.

4 UHF-band results

The MeerKLASS OTF UHF survey constitutes the largest wide-area interferometric imaging effort using fast-scanning data from MeerKAT's 544–1088 MHz band. It provides a unique window on the faint radio sky, bridging classical L-band extragalactic surveys and the low-frequency regime probed by instruments such as LOFAR and MWA. The overarching objective of the MeerKLASS UHF survey is to deliver a deep, wide-area, high-resolution radio continuum map of the southern sky while running fully commensally with the single-dish H I intensity-mapping experiment.

The first data release (DR1, Paul et al. 2025) focuses on a subset of approximately 800 deg^2 obtained from eight OTF observing blocks (corresponding to ~12 h of total integration). The footprint overlaps the DESI extragalactic field and serves as a pilot region for future survey expansion. We divided the survey area into 89 individual tiles for imaging (each $\approx 3^\circ \times 3^\circ$). Direction-independent imaging and self-calibration were performed with DDFacet using robust 0 weighting. The resulting continuum mosaic (Fig. 8) reaches a sensitivity of $\approx 35\ \mu$Jy beam^{-1} in regions with contribution from 8 datablocks and a median synthesized beam of $32'' \times 17''$ (FWHM). The achieved depth is consistent with thermal-noise expectations for the cumulative integration time, demonstrating that stable, high-fidelity imaging is attainable despite the intrinsic motion of the OTF scanning strategy.

Figure 8 provides a global view of the continuum image quality across the entire 800 deg^2 footprint. The top panel displays a composite mosaic constructed from the restored images of 89 individual tiles. This full-field image was assembled using Montage[5], which reprojects each input FITS image to a common WCS frame before co-adding them into a seamless large-area mosaic. To produce this, we first collected the final restored images for all tiles, each corresponding to a $3.2^\circ \times 3.2^\circ$ field generated by a single DDFacet imaging run. All tiles share a common pixel scale of 3 arcsec and are aligned in equatorial coordinates. The bottom panel shows a zoomed in view of the survey center. Figure 9 shows a comparison of M-OTF image with RACS-Low (Hale et al., 2021), NVSS (Condon et al., 1998) and TGSS-ADR (Intema et al., 2017). These demonstrate the high image quality achieved across the survey, revealing numerous compact and extended sources, clean background regions, and minimal residual artefacts. Source extraction with PyBDSF yields a catalog of $\sim 10^5$ sources at a 7σ threshold. Morphological statistics indicate that the population is largely marginally resolved. The total-to-peak flux-density ratio (T/P) declines from ~ 1.12 at SNR ~ 10 to ~ 1.03 by SNR $\sim 10^3$, and the resolved fraction similarly decreases with SNR, consistent with a catalog dominated by compact sources and minimal resolution bias at high SNR.

Differential source counts derived from DR1 are in good agreement with existing wide surveys (e.g. RACS-Low, NVSS) after frequency scaling to a representative UHF band centre (816 MHz), supporting both the photometric fidelity and the completeness of the catalog above ~ 1 mJy. Astrometric offsets are well below the $3''$ pixel scale, and fluxes agree with external surveys within expected spectral and resolution systematics. Collectively, these results validate OTF interferometric imaging as a robust and efficient mode for wide-field radio continuum surveys.

5 L-band results

The MeerKLASS L-band survey employs the fast-scanning OTF observations to cover approximately ~270 deg^2 of sky across the $856 - 1712$ MHz band. This initial data release (DR1, Mangla et al. 2025) is compiled from 67 individually processed image tiles, with each tile covering an area of $\approx 2^\circ \times 2^\circ$ on the sky. The survey's footprint provides significant overlap with existing wide-area optical surveys, such as Kilo-Degree Survey (KiDS-DR5, Wright et al. (2024)), providing a valuable multi-wavelength dataset.

Following the process described in section 3, the resulting map has an excellent, consistent quality, achieving an average rms noise level of $\approx 34\,\mu$Jy across the entire field. The median resolution of a synthesized beam is $26'' \times 8''$. The achieved imaging depth aligns precisely with the expectations from the thermal noise limit for the cumulative observing time, thus validating the efficiency and

---

[5] `http://montage.ipac.caltech.edu`

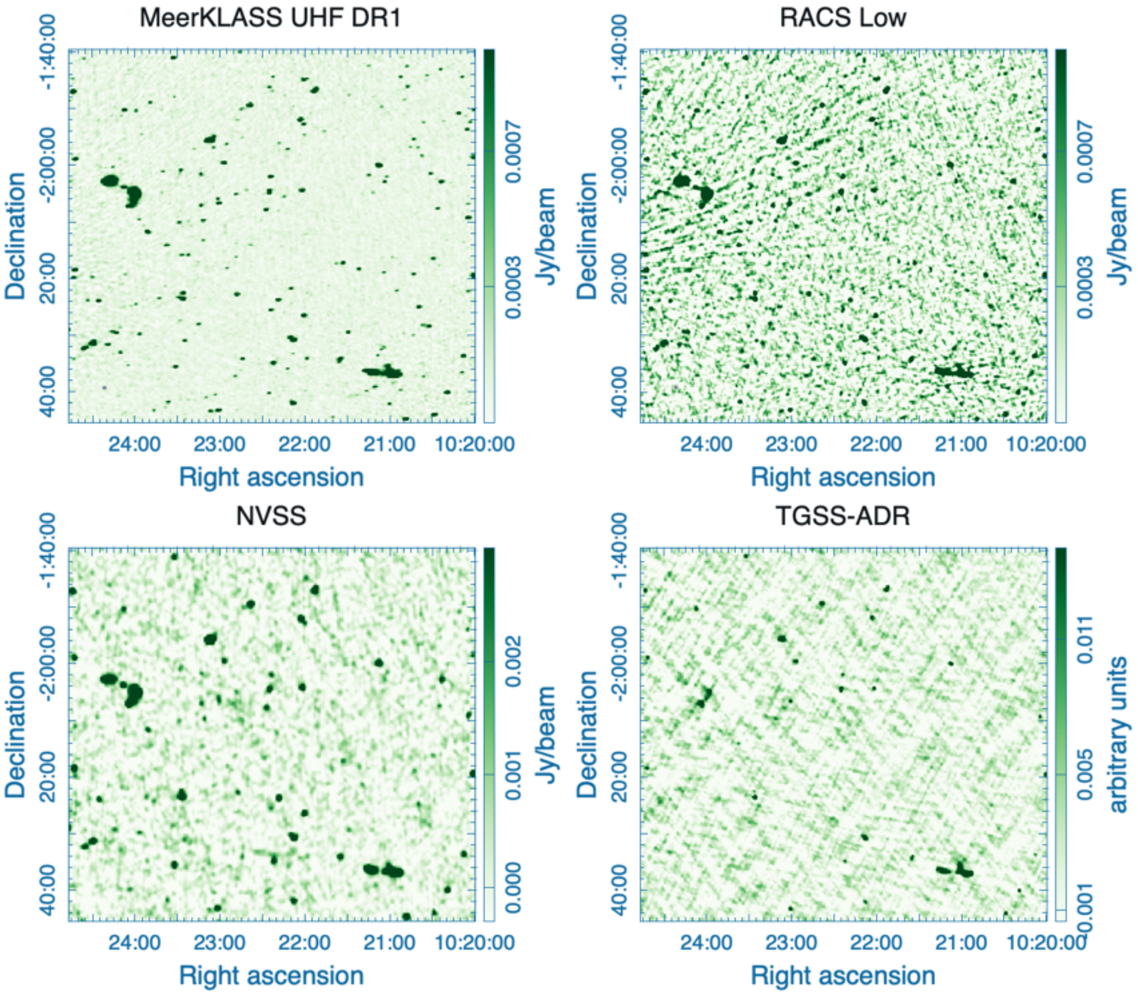

Figure 9: Comparison of the MeerKLASS UHF-band image with major radio surveys. Flux-density scales differ between panels and are set by each survey's sensitivity (see Table 1). The MeerKLASS UHF-band DR1 image reveals substantially fainter sources than the other surveys.

robustness of the OTF observing strategy. A representative section of the resulting continuum image, which highlights the high quality and low noise floor achieved, is shown in Figure 10.

Source detections was performed using the PyBDSF source finding algorithm, yielding over 40,000 sources detected above S/N threshold of 9. This catalog is estimated to be over 90% complete above a flux density of 0.6 mJy. To confirm the photometric and astrometric fidelity of the source measurements, the properties of the detected sources were cross-matched against established external radio surveys, including the NVSS, TGSS-ADR, and the ASKAP-RACS catalogs (Low, Mid, and High). Comparison with the RACS-mid is illustrated in Figure 11, confirming the consistency of the MeerKLASS flux scale. We found that the astrometric positions are highly accurate, with positional errors being less than 1.5″ (the map's pixel size). Furthermore, the flux density measurements agree with those from external surveys to within a 2-3 per cent uncertainty. This agreement is based on a global fit to the results from all common detected sources between the

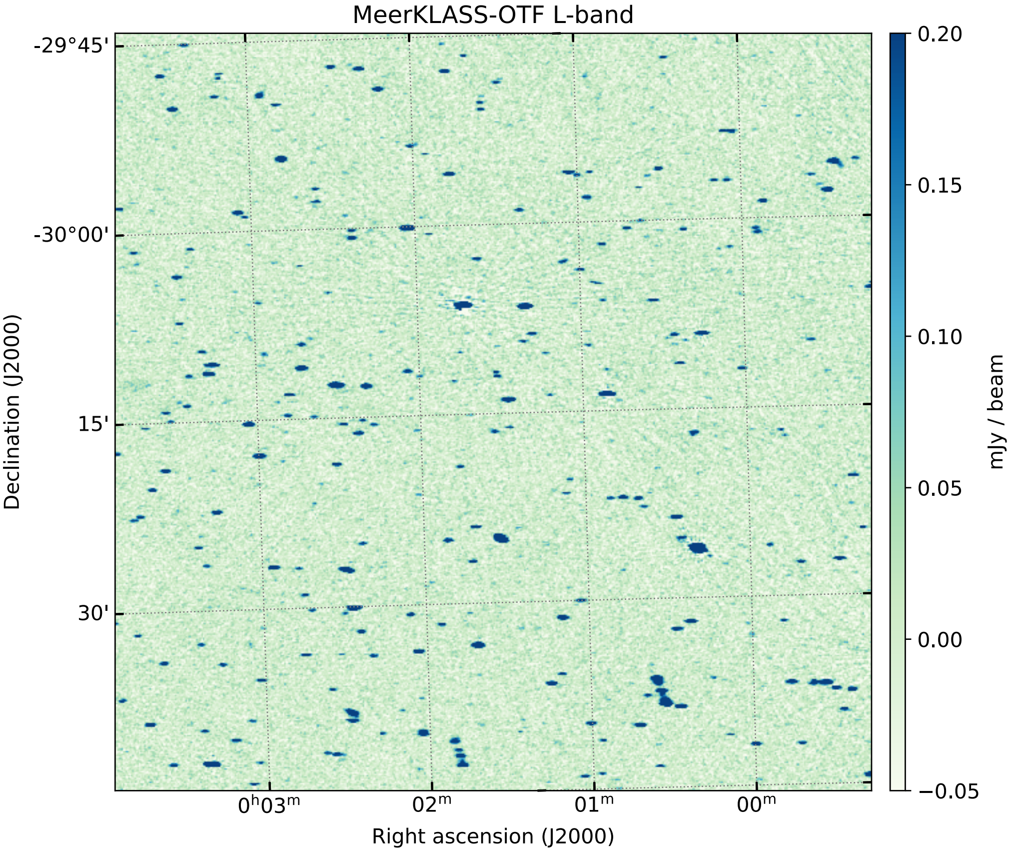

Figure 10: MeerKLASS L-band image at 1.284 GHz, covering a one square degree field. The map reaches an RMS noise of 32.6 μJy/beam. The restoring beam is $26'' \times 7.8''$, giving the elongated resolution pattern you see in the map.

surveys, after applying frequency corrections based on a typical synchrotron spectrum ($S_\nu \propto \nu^\alpha$ with $\alpha = -0.7$). Collectively, these initial results validate the OTF imaging technique as a dependable and efficient method for executing wide-scale radio surveys with a successfully achieved low noise floor.

6 Predictions for SKA-Mid

In this section we discuss our forecast from SKA-Mid OTF observations. Considering SKA-Mid is a general purpose telescope, a good all-sky radio source model is an absolute necessity. The OTF mapping technique developed using SKA-Mid pathfinder telescope MeerKAT has a high survey speed, able to achieve uniform sensitivity over a large sky area and can be performed in a commensal observation with H I IM experiments. This makes the OTF mapping suitable for all-sky model building and long period transient search.

For the forecast, we have assumed SKA-Mid telescope will be deployed in three stages. In the first stage, all the existing 64 MeerKAT dishes will be updated to SKA-Mid specifications. Second stage (SKA-Mid AA*) will be a combination of 80 dishes with 15 m diameter and 64 dishes with

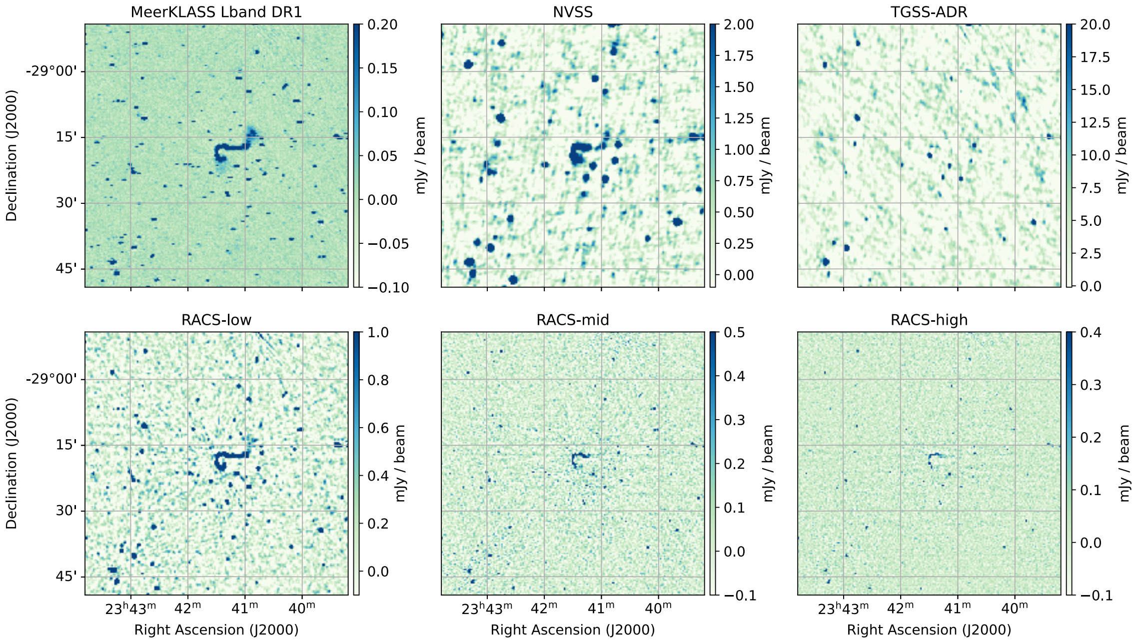

Figure 11: Comparison of the MeerKLASS L-band image with major radio surveys. Top panel: MeerKLASS L-band DR1 image with NVSS and TGSS-ADR overlaid for the same sky region. Lower panels: RACS-low, RACS-mid, and RACS-high images of the same field. Flux-density scales differ between panels and are set by each survey's sensitivity (see Table 1). The MeerKLASS L-band DR1 image reveals substantially fainter sources and more extended emission than the other surveys.

Configuration	MeerKAT	SKA-Mid (64 MeerKAT)	SKA-Mid (AA*)	SKA-Mid (AA4)
Dishes	58	64	80+64	133+64
Synthesize Beam	$14.4''$	$15.89'' \times 10.69''$	$3.49'' \times 2.94''$	$1.32'' \times 1.14''$
Stokes I snapshot noise (2-second) in μJy/beam	277	343	142.6	100
Stokes I one epoch noise (18-seconds / sq. deg) in μJy/beam	104	114	48	33
Stokes I 26 epoch noise in μJy/beam	35	30	9	7

Table 2: The table shows forecast for OTF mapping with SKA-Mid.

13.5 m diameter. Finally, the third stage (SKA-Mid AA4) will contain 133 dishes of 15 m diameter along with the 64 MeerKAT dishes. The new 15 m dishes will help SKA-Mid to reach high angular resolution while remaining sensitive for large-scale emission due to the existing dens coverage of baseline ≤ 1Km.

Table 2 shows the forecast for OTF mapping with SKA-Mid. For completeness, we have also included existing MeerKAT predictions to the table also. From our current OTF setup, we combine about 9 snapshots per square degree per epoch to perform visibility plane mosaicking, and we have used this for the forecast. For uniformity, we have assumed that 70% of the observed data is usable. It is worth noting that our current M-OTF observations are performed at night only, and we find that about 15% data from the fast-scan is being flagged. This number can vary day-to-day basis, but rms estimates in the table shown here are poorer than what we actually see. Further following our current M-OTF plan, we assume that we will be combining 26 epochs per box with SKA-Mid. Using this rather pessimistic scenario, we expect to achieve an rms of 9 μJy/beam with a resolution of $3.2''$ using AA* and 7μJy/beam with a resolution of $1.2''$ using AA4 (Figure 1). Further, we expect the SKA-Mid setup will be able to update the delay center at an interval of 0.5-seconds, making the OTF mapping practically smearing free. However, combining two different antenna design may pose some challenge toward imaging and flux-scale accuracy. Investigates are going on to asses the impact of this and will be addressed in future studies.

7 Summary

MeerKLASS is an H I intensity mapping survey that aims to detect the 21cm power spectrum from redshift < 1.44. Alongside the auto-correlation (single dish) visibilities, MeerKLASS also records interferometric visibilities in On-The-Fly (OTF) mode. In this work, we introduce the MeerKLASS OTF (M-OTF) survey. We have developed and tested a new calibration and imaging capability for MeerKAT in which antennas are moved back-and-forth at a constant elevation and the visibilities are recorded continuously at 2s interval. This commensal continuum observation significantly reduces the slew-and-settle overhead compared to a traditional tracking observation. As a consequence we achieve a high survey speed of 15 $\mathrm{deg^2 hr^{-1}}$ to achieve a noise of 25 $\mu\mathrm{Jybeam^{-1}}$ in the UHF band.

We have developed an end-to-end pipeline that flags, calibrates, performs OTF correction and stores the visibilities in 2s snapshot measurement sets. The relevant steps of this process are described in detail in section 2. These 2s snapshot measurement sets are independent, and standard imaging techniques can be used to produce 2s snapshot images. These are crucial for slow transient search. However, there are limitations to M-OTF observations. In the current format, the delay center of the observation is fixed during the scanning process, whereas the telescope pointing performs a horizontal raster scan, and the earth rotates. This introduces a smearing that affects our images significantly (section 3). To overcome these limitations, we have incorporated a smearing correction during the imaging, where the dirty image is deconvolved using a smeared PSF that constructs a correct sky model. Due to this correction, the resolution of the images go down (subsection 3.4).

In principle, the 2s images can be combined to achieve a deeper image that is required for producing a source catalog and other scientific objectives. But that limits our ability to deconvolve faint sources. To overcome this, we have used `DDFacet` to perform joint deconvolution (visibility plane mosaicking) in our imaging pipeline. Further, we have performed a thorough investigation of the source flux, positional accuracy by comparing with other overlapping available catalogs. We compare the astrometry and flux-density measurements of MeerKLASS catalog with RACS-Mid. This comparison shows that astrometric offsets are typically constrained to within a pixel of the M-OTF data. Comparison of source flux densities show agreement with RACS-Mid observations at high SNR, whereas the scatter in the flux-density comparison increases at low SNR regime while maintaining the average one-to-one trend.

MeerKLASS OTF survey is an ideal example of a commensal survey where the telescope time is utilized for multiple science drivers. This potentially be helpful for producing large area sky models and slow transient searches with the upcoming SKA-Mid. In section 6 we have discussed the expected sensitivity and resolution achievable with different proposed stages of SKA-Mid. We find that with SKA-Mid AA4 configuration, we can achieve an rms of 7 μJybeam^{-1} at a resolution of 1.2$''$. However, it is difficult to estimate the impact of combining visibility measurement from two different type of antennas and more tests are going on to asses this.

References

D. Alonso et al. *Monthly Notices of the Royal Astronomical Society*, 502(1):876–887, 01 2021. ISSN 0035-8711. doi: 10.1093/mnras/stab046. URL `https://doi.org/10.1093/mnras/stab046`.

W. Baan. *PoS*, RFI2010:001, 2010. doi: 10.22323/1.107.0001.

R. Braun et al. Anticipated performance of the square kilometre array – phase 1 (ska1), 2019. URL `https://arxiv.org/abs/1912.12699`.

S. Chatterjee et al. *arXiv e-prints*, art. arXiv:2512.11978, Dec. 2025. doi: 10.48550/arXiv.2512.11978.

M. Collaboration et al. *Monthly Notices of the Royal Astronomical Society*, 537(4):3632–3661, 02 2025. ISSN 0035-8711. doi: 10.1093/mnras/staf195. URL `https://doi.org/10.1093/mnras/staf195`.

J. J. Condon et al. *AJ*, 115(5):1693–1716, May 1998. doi: 10.1086/300337.

S. Cunnington et al. *MNRAS*, 518(4):6262–6272, 10 2022. ISSN 0035-8711. doi: 10.1093/mnras/stac3060. URL `https://doi.org/10.1093/mnras/stac3060`.

S. Cunnington et al. Revealing cosmological fluctuations in 21cm intensity maps with meerklass: from maps to power spectra, 2025. URL `https://arxiv.org/abs/2510.27549`.

S. Cunnington et al. In *Advancing Astrophysics with the SKA – II (AASKAII)*. 2026. arXiv search: Report number AASKAII/Cunnington01.

de Gasperin, F. et al. *AA*, 673:A165, 2023. doi: 10.1051/0004-6361/202245389. URL `https://doi.org/10.1051/0004-6361/202245389`.

S. Duchesne et al. *arXiv preprint arXiv:2501.04978*, 2025.

S. W. Duchesne et al. *Publications of the Astronomical Society of Australia*, 40, 2023. ISSN 1448-6083. doi: 10.1017/pasa.2023.31. URL `http://dx.doi.org/10.1017/pasa.2023.31`.

B. N. Engelbrecht et al. *Monthly Notices of the Royal Astronomical Society*, 536(1):1035–1055, 11 2024. ISSN 0035-8711. doi: 10.1093/mnras/stae2649. URL `https://doi.org/10.1093/mnras/stae2649`.

N. Gupta et al. In *MeerKAT Science: On the Pathway to the SKA*, page 14, Jan. 2016. doi: 10.22323/1.277.0014.

C. Hale and F. Tabatabaei. In *Advancing Astrophysics with the SKA – II (AASKAII)*. 2026. arXiv search: Report number AASKAII/Hale01.

C. L. Hale et al. *Publications of the Astronomical Society of Australia*, 38, 2021. ISSN 1448-6083. doi: 10.1017/pasa.2021.47. URL http://dx.doi.org/10.1017/pasa.2021.47.

C. L. Hale et al. *Monthly Notices of the Royal Astronomical Society*, 527(3):6540–6568, 10 2023. ISSN 0035-8711. doi: 10.1093/mnras/stad3088. URL https://doi.org/10.1093/mnras/stad3088.

S. E. Harper and C. Dickinson. *Monthly Notices of the Royal Astronomical Society*, 479(2):2024–2036, 06 2018. ISSN 0035-8711. doi: 10.1093/mnras/sty1495. URL https://doi.org/10.1093/mnras/sty1495.

I. Harrison et al. In *Advancing Astrophysics with the SKA – II (AASKAII)*. 2026. arXiv search: Report number AASKAII/Spinelli02.

C. G. T. Haslam, C. J. Salter, H. Stoffel, and W. E. Wilson. *A&AS.*, 47:1, Jan. 1982.

A. Hopkins et al. *Publications of the Astronomical Society of Australia*, 42:e071, 2025. doi: 10.1017/pasa.2025.10042.

B. V. Hugo et al. In J. E. Ruiz, F. Pierfedereci, and P. Teuben, editors, *Astronomical Data Analysis Software and Systems XXX*, volume 532 of *Astronomical Society of the Pacific Conference Series*, page 541, July 2022. doi: 10.48550/arXiv.2206.09179.

N. Hurley-Walker et al. *Monthly Notices of the Royal Astronomical Society*, 464(1):1146–1167, 09 2016. ISSN 0035-8711. doi: 10.1093/mnras/stw2337. URL https://doi.org/10.1093/mnras/stw2337.

H. T. Intema, P. Jagannathan, K. P. Mooley, and D. A. Frail. *A&A*, 598:A78, 2017. doi: 10.1051/0004-6361/201628536. URL https://doi.org/10.1051/0004-6361/201628536.

J. Jonas and MeerKAT Team. In *MeerKAT Science: On the Pathway to the SKA*, page 1, Jan. 2016. doi: 10.22323/1.277.0001.

G. I. G. Józsa et al. In R. Pizzo et al., editors, *Astronomical Data Analysis Software and Systems XXIX*, volume 527 of *Astronomical Society of the Pacific Conference Series*, page 635, Jan. 2020. doi: 10.48550/arXiv.2006.02955.

M. Lacy et al. *Publications of the Astronomical Society of the Pacific*, 132(1009):035001, jan 2020. doi: 10.1088/1538-3873/ab63eb. URL https://dx.doi.org/10.1088/1538-3873/ab63eb.

S. Mangla et al. *arXiv e-prints*, art. arXiv:2512.17685, Dec. 2025. doi: 10.48550/arXiv.2512.17685.

J. G. Mangum, D. T. Emerson, and E. W. Greisen. *A&A*, 474(2):679–687, Nov. 2007. doi: 10.1051/0004-6361:20077811.

T. Mauch et al. *Monthly Notices of the Royal Astronomical Society*, 342(4):1117–1130, 07 2003. ISSN 0035-8711. doi: 10.1046/j.1365-8711.2003.06605.x. URL `https://doi.org/10.1046/j.1365-8711.2003.06605.x`.

D. McConnell et al. *Publications of the Astronomical Society of Australia*, 37, 2020. ISSN 1448-6083. doi: 10.1017/pasa.2020.41. URL `http://dx.doi.org/10.1017/pasa.2020.41`.

K. P. Mooley et al. *The Astrophysical Journal*, 870(1):25, dec 2018. doi: 10.3847/1538-4357/aaef7c. URL `https://dx.doi.org/10.3847/1538-4357/aaef7c`.

T. Murphy et al. *Monthly Notices of the Royal Astronomical Society*, 402(4):2403–2423, 03 2010. ISSN 0035-8711. doi: 10.1111/j.1365-2966.2009.15961.x. URL `https://doi.org/10.1111/j.1365-2966.2009.15961.x`.

R. P. Norris et al. *Publications of the Astronomical Society of Australia*, 28(3):215–248, 2011. doi: 10.1071/AS11021.

A. R. Offringa et al. *MNRAS*, 405(1):155–167, June 2010. doi: 10.1111/j.1365-2966.2010.16471.x.

S. Paul et al. The meerklass uhf on-the-fly continuum survey – data release i, 2025. URL `https://arxiv.org/abs/2512.11964`.

M. G. Santos et al. In *Proceedings, MeerKAT Science: On the Pathway to the SKA (MeerKAT2016): Stellenbosch, South Africa, May 25-27, 2016*, 2017.

T. Sawada et al. *PASJ*, 60:445, June 2008. doi: 10.1093/pasj/60.3.445.

Shimwell, T. W. et al. *A&A*, 659:A1, 2022. doi: 10.1051/0004-6361/202142484. URL `https://doi.org/10.1051/0004-6361/202142484`.

O. M. Smirnov. *A&A*, 527:A107, Mar. 2011. doi: 10.1051/0004-6361/201116434.

C. Tasse et al. *Astronomy amp; Astrophysics*, 611:A87, Mar. 2018. ISSN 1432-0746. doi: 10.1051/0004-6361/201731474. URL `http://dx.doi.org/10.1051/0004-6361/201731474`.

Wagenveld, J. D. et al. *AA*, 690:A163, 2024. doi: 10.1051/0004-6361/202450291. URL `https://doi.org/10.1051/0004-6361/202450291`.

J. Wang et al. *Monthly Notices of the Royal Astronomical Society*, 505(3):3698–3721, 05 2021. ISSN 0035-8711. doi: 10.1093/mnras/stab1365. URL `https://doi.org/10.1093/mnras/stab1365`.

R. B. Wayth et al. *Publications of the Astronomical Society of Australia*, 32:e025, 2015. doi: 10.1017/pasa.2015.26.

A. H. Wright et al. *AAP*, 686:A170, June 2024. doi: 10.1051/0004-6361/202346730.